Chem

CellPress

Article

Subnanometric Hybrid Pd-M$(OH)_2$, M = Ni, Co, Clusters in Zeolites as Highly Efficient Nanocatalysts for Hydrogen Generation

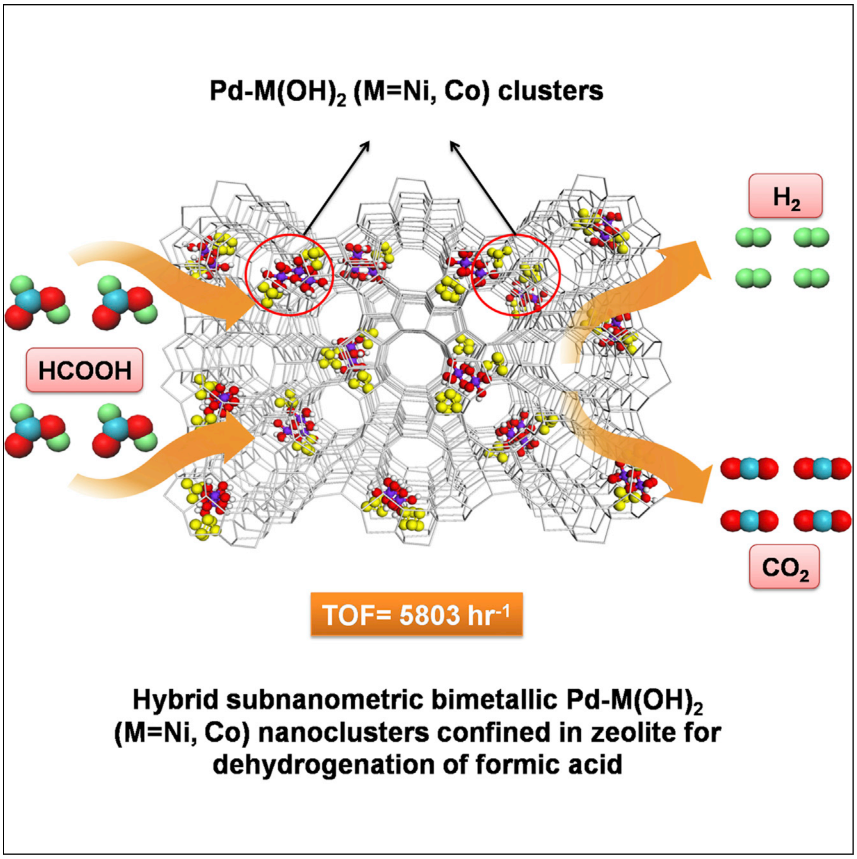

Qiming Sun, Ning Wang,
Qiming Bing, ..., Peng Zhang,
Mingjun Jia, Jihong Yu

jihong@jlu.edu.cn

HIGHLIGHTS

Synthesis of subnanometric hybrid bimetallic clusters within zeolites

The nanocatalysts possessed excellent activity for hydrogen generation

The nanocatalysts exhibited shape-selective catalytic performance

The nanocatalysts showed superior thermal stability and recyclability

Subnanometric hybrid bimetallic palladium-transition metal hydroxide clusters are encapsulated within zeolites by using metallic ethylenediamine complexes as precursors under direct hydrothermal conditions. The hybrid bimetallic nanocatalysts exhibit shape-selective catalytic performance, superior thermal stability, as well as exceedingly high dehydrogenation efficiency toward complete formic acid decomposition as a result of the nanoconfinement effect of zeolites as well as the synergistic effect of hybrid metal species.

7 AFFORDABLE AND CLEAN ENERGY

Sun et al., Chem *3*, 1–17
September 14, 2017
http://dx.doi.org/10.1016/j.chempr.2017.07.001

Please cite this article in press as: Sun et al., Subnanometric Hybrid Pd-M(OH)$_2$, M = Ni, Co, Clusters in Zeolites as Highly Efficient Nanocatalysts for Hydrogen Generation, Chem (2017), http://dx.doi.org/10.1016/j.chempr.2017.07.001

Chem

CellPress

Article

Subnanometric Hybrid Pd-M(OH)$_2$, M = Ni, Co, Clusters in Zeolites as Highly Efficient Nanocatalysts for Hydrogen Generation

Qiming Sun,[1,7] Ning Wang,[1,7] Qiming Bing,[2] Rui Si,[3] Jingyao Liu,[2] Risheng Bai,[1] Peng Zhang,[4] Mingjun Jia,[5] and Jihong Yu[1,6,8,*]

SUMMARY

Hybrid multi-metallic nanocatalysts have attracted increasing attention because of the synergistic effect of metal species and considerably improved catalytic performance, but they often suffer from severe sintering and poor stability. Here, we show a facile strategy for preparing subnanometric hybrid bimetallic clusters Pd-M(OH)$_2$ (M = Ni, Co) within silicalite-1 (S-1) zeolite via a hydrothermal synthesis method. The hybrid bimetallic nanocatalysts exhibit excellent shape-selective catalytic performance and superior thermal stability. The incorporation of secondary Ni(OH)$_2$ species in S-1 can considerably increase the catalytic activity of the Pd nanoclusters for the dehydrogenation of formic acid (FA) as a result of the electron-enriched Pd surface and bimetallic interfacial effect. Notably, the 0.8Pd0.2Ni(OH)$_2$@S-1 catalyst affords the highest initial turnover frequency value, up to 5,803 hr^{-1} toward complete FA decomposition without any additives at 60°C. The superior catalytic properties and excellent stability of the subnanometric hybrid bimetallic clusters confined in zeolites create new prospects for their practical high-performance catalytic application.

INTRODUCTION

Supported metal clusters have been widely used in diverse heterogeneous catalysis reactions for many important industrial processes, such as petroleum refining, hydrogenation, and conversion of automobile exhaust.[1–5] The size of the metal clusters is a critical factor in determining the performance of such catalysts.[6] In general, smaller metal clusters, especially those of subnanometric[7,8] or even single atom[9–11] size possess unique and improved catalytic properties compared with larger metal clusters because of more accessibly exposed active sites and enhanced charge transfer between the metal species and supports. Recently, hybrid multi-metal nanoparticles have attracted widespread attention for their significantly improved catalytic activity, which arises from the superior synergistic effect of their multi-component interfacial active sites.[12–16] Notably, introduction of non-noble metal hydroxides to form multi-metallic nanostructures can not only minimize the use of noble metal but also enhance the catalytic performance.[12–15] For example, hybrid Pt/FeNi(OH)$_x$ nanoparticles exhibited highly efficient performance for CO oxidation,[12] and Pt/M(OH)$_2$ (M = Ni, Co) nanoparticles can greatly enhance the activity of the H$_2$ evolution reaction.[14] However, small multi-metal nanoparticles, especially non-noble metal-containing nanoparticles, tend to suffer from severe aggregation, poor hydrothermal stability, and high metal leaching during catalytic reaction or thermal treatment because of their

The Bigger Picture

Hybrid multi-metallic nanocatalysts have attracted increasing attention because of the synergistic effect of metal species and considerably improved catalytic activity but often suffer from severe sintering and poor stability. Zeolites are known as ideal supports for confinement synthesis of metal nanoparticles. In this work, subnanometric hybrid Pd-M(OH)$_2$ (M = Ni, Co) clusters encapsulated within purely siliceous zeolites were synthesized via a hydrothermal synthesis method. The hybrid bimetallic nanocatalysts exhibit superior thermal stability at 600°C–700°C and afford the highest initial turnover frequency value, up to 5,803 hr^{-1} toward complete formic acid decomposition without any additives at 60°C. The hybrid bimetallic nanoclusters confined in zeolites have potential practical application in dehydrogenation of formic acid as a viable and effective chemical hydrogen storage medium for fuel cells, and also raise more possibilities for other important high-performance catalytic reactions.

Please cite this article in press as: Sun et al., Subnanometric Hybrid Pd-M(OH)$_2$, M = Ni, Co, Clusters in Zeolites as Highly Efficient Nanocatalysts for Hydrogen Generation, Chem (2017), http://dx.doi.org/10.1016/j.chempr.2017.07.001

considerable increase in surface free energy at smaller sizes. Generation of multi-metal nanoparticles, especially non-noble metal hydroxide-containing multi-metallic nanoparticles with ultrasmall particle size and excellent thermal stability, is still a great challenge.

Zeolites with ordered micropores (<2 nm), well-defined crystal structure, and high hydrothermal stability are the ideal supports for confinement synthesis of metal nanoparticles.[17–21] The zeolite matrix can protect nanoparticles against aggregation, thereby enhancing their catalytic activity and stability. Unfortunately, metal nanoparticles deposited onto zeolites using conventional ion-exchange and wetness impregnation methods tend to form non-uniform metal particles with large particle sizes and exhibit poor thermal stability, resulting in suboptimal catalytic activity.[22] Lately, Iglesia and co-workers developed ligand-stabilized methods for encapsulating series of small noble mono-/bimetal clusters (1–2 nm) into microporous cavities of different aluminosilicate zeolites.[23–27] However, introducing Al into zeolites may restrict the catalytic application of these materials because of the resultant undesirable acidity and decreased hydrothermal stability. Notably, Liu et al.[8] prepared subnanometric Pt clusters within purely siliceous MCM-22 (**MWW** zeotype) zeolite during the growth of a two-dimensional zeolite into three dimensions. The catalysts exhibited exceptional high stability and shape-selective catalytic performance but suffered from 70% weight loss of Pt after oxidation-reduction treatments.[28] Very recently, we have developed a facile method to synthesize ultrasmall Pd clusters encapsulated within purely siliceous silicalite-1 (S-1) zeolite (**MFI**) by using $[Pd(NH_2CH_2CH_2NH_2)_2]Cl_2$ as precursor under direct hydrothermal conditions.[29] The as-synthesized catalyst exhibited excellent catalytic activity for the dehydrogenation of formic acid (FA) in portable fuel cell applications as well as superior stability as a result of the well-confined Pd clusters within the silica zeolite matrix. Recently, Dai et al.[30–33] successfully encapsulated some mono-/bimetallic (oxide) nanoparticles inside the hollow zeolites by a top-down dissolution-recrystallization method. However, until now, there has been no report of ultrasmall non-noble metal hydroxide-containing multi-metallic nanoclusters *in situ* confined within purely siliceous zeolites that are capable of promoting catalytic performance and thermal stability.

In this work, we have demonstrated a facile and one-pot synthesis strategy to prepare subnanometric hybrid bimetallic clusters Pd-M(OH)$_2$ (M = Ni, Co) confined within purely siliceous S-1 zeolite nanocrystals using metallic ethylenediamine complex mixtures as precursors via a hydrothermal synthesis method. The subnanometric sizes of the hybrid bimetallic Pd and Ni(OH)$_2$ clusters were confirmed using scanning transmission electron microscopy (STEM) and extended X-ray absorption fine structure (EXAFS) analyses. The nanocatalysts obtained demonstrated superior thermal stability under industrial conditions and excellent shape-selective catalytic performance. Most significantly, 0.8Pd0.2Ni(OH)$_2$@S-1 afforded exceedingly high initial and total turnover frequency (TOF) values up to 5,803 hr^{-1} and 1,879 hr^{-1} for the complete decomposition of FA; notably these TOF values were achieved without generating CO, without using any additive at 60°C, making this among the highest activities for heterogeneously catalyzed FA decomposition under similar conditions.[34–36] The superior catalytic performance, excellent thermal stability, and recyclability of hybrid non-noble metal hydroxide-containing bimetallic clusters confined in zeolites not only facilitate their practical application in the dehydrogenation of FA as a viable and effective chemical hydrogen storage medium for fuel cells but also provide opportunities for other important high-performance catalytic reactions.

---

[1] State Key Laboratory of Inorganic Synthesis and Preparative Chemistry, College of Chemistry, Jilin University, Changchun 130012, People's Republic of China

[2] Laboratory of Theoretical and Computational Chemistry, Institute of Theoretical Chemistry, Jilin University, Changchun 130023, People's Republic of China

[3] Shanghai Synchrotron Radiation Facility, Shanghai Institute of Applied Physics, Chinese Academy of Sciences, Shanghai 201204, People's Republic of China

[4] Department of Chemistry, Dalhousie University, Halifax, NS B3H 4R2, Canada

[5] Key Laboratory of Surface and Interface Chemistry of Jilin Province, College of Chemistry, Jilin University, Changchun 130021, People's Republic of China

[6] International Center of Future Science, Jilin University, Changchun 130012, People's Republic of China

[7] These authors contributed equally

[8] Lead Contact

*Correspondence: jihong@jlu.edu.cn

http://dx.doi.org/10.1016/j.chempr.2017.07.001

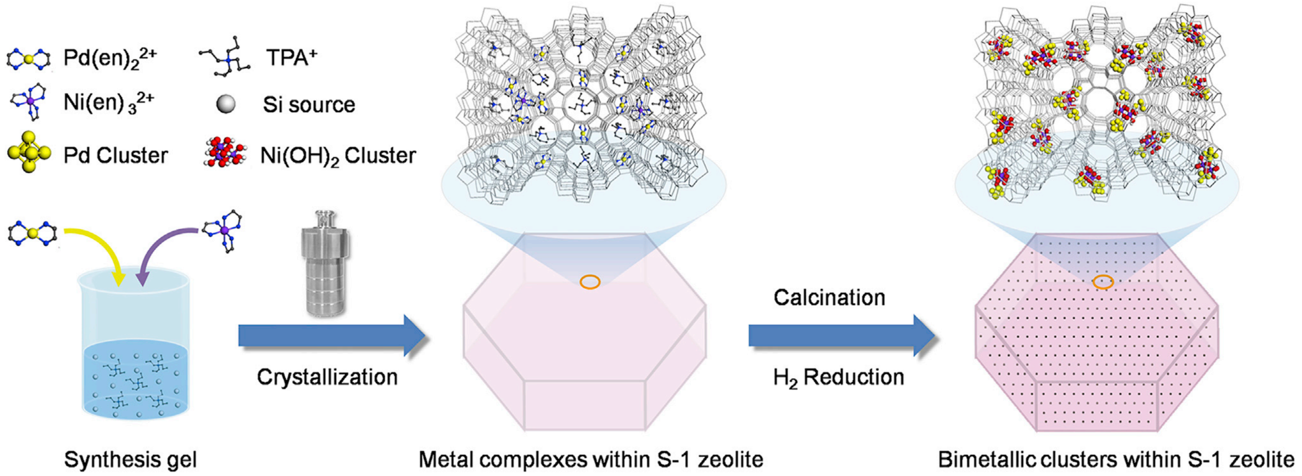

Figure 1. Schematics of the Preparation of Hybrid Bimetallic Pd-Ni(OH)$_2$@S-1 Catalyst

$Pd(en)_2^{2+}$ and $Ni(en)_3^{2+}$ complexes are added into the synthetic gel, and the gel is then crystallized in the autoclave under conventional hydrothermal conditions at 170°C for 4 days. The metal complexes interact with the initial zeolitic gel and are encapsulated within the zeolite framework during the crystallization process. After calcination in air and reduction by H_2, the subnanometric Pd-Ni(OH)$_2$ clusters are finally confined inside the nanosized S-1 zeolite.

RESULTS AND DISCUSSION

Synthesis and Characterization of Pd-Ni(OH)$_2$@S-1 Samples

The overall synthesis of subnanometric bimetallic Pd-Ni(OH)$_2$ clusters encapsulated within nanosized S-1 zeolites (denoted as xPd(1 − x)Ni(OH)$_2$@S-1) is illustrated in Figure 1. For comparison, monometallic Pd@S-1 and Ni(OH)$_2$@S-1 samples were also prepared under similar conditions. X-ray diffraction analysis of all samples confirmed the intended **MFI** zeolite structure, indicating that the introduction of additional metal species did not interfere with zeolite crystallization (Figure S1). Inductively coupled plasma atomic emission spectroscopy (ICP-AES) analysis confirmed that all the bimetallic samples possessed similar total metal loading amounts (0.63–0.64 wt %). The molar ratios of Pd/Ni in the products were 0.91/0.09, 0.83/0.17, and 0.73/0.27, respectively, in accordance with those in the initial gels (Table S1).

Scanning electron microscopy (SEM) and transmission electron microscopy (TEM) images show that the metal clusters are uniformly distributed throughout the nanosized S-1 zeolite crystals (200–300 nm) (Figures S2 and S3). The visually observed average bimetallic clusters sizes in all of the samples are ~1.7 nm, similar to those of the monometallic Pd and Ni(OH)$_2$ clusters. Those bimetallic cluster sizes are much smaller than those formed in the Pd/S-1-im and Pd-Ni(OH)$_2$/S-1-im (~2.9 nm) catalysts prepared with the impregnated method, as well as those formed in the Pd@S-1/Ni(OH)$_2$-im catalysts by impregnating Ni(NO$_3$)$_2$ solution into Pd@S-1 catalyst (~3.3 nm) (Figures S4 and S5). The ultrasmall diameters and monodispersed size distributions of bimetallic clusters in these zeolites indicate that the *in situ* confinement of metal clusters in zeolite matrices can effectively inhibit aggregation of the metal clusters. N_2 adsorption-desorption analyses reveal that about 200 m^2/g of micropore area and 0.10 cm^3/g of micropore volume exist in metal-containing samples, ensuring sufficient diffusion for the reactant, with only about 30 m^2/g and 0.01 cm^3/g decrease in micropore area and micropore volume compared with the S-1 zeolite, as a result the partial occupation of metal species in the channels of zeolites (Figure S6 and Table S1).

Please cite this article in press as: Sun et al., Subnanometric Hybrid Pd-M(OH)$_2$, M = Ni, Co, Clusters in Zeolites as Highly Efficient Nanocatalysts for Hydrogen Generation, Chem (2017), http://dx.doi.org/10.1016/j.chempr.2017.07.001

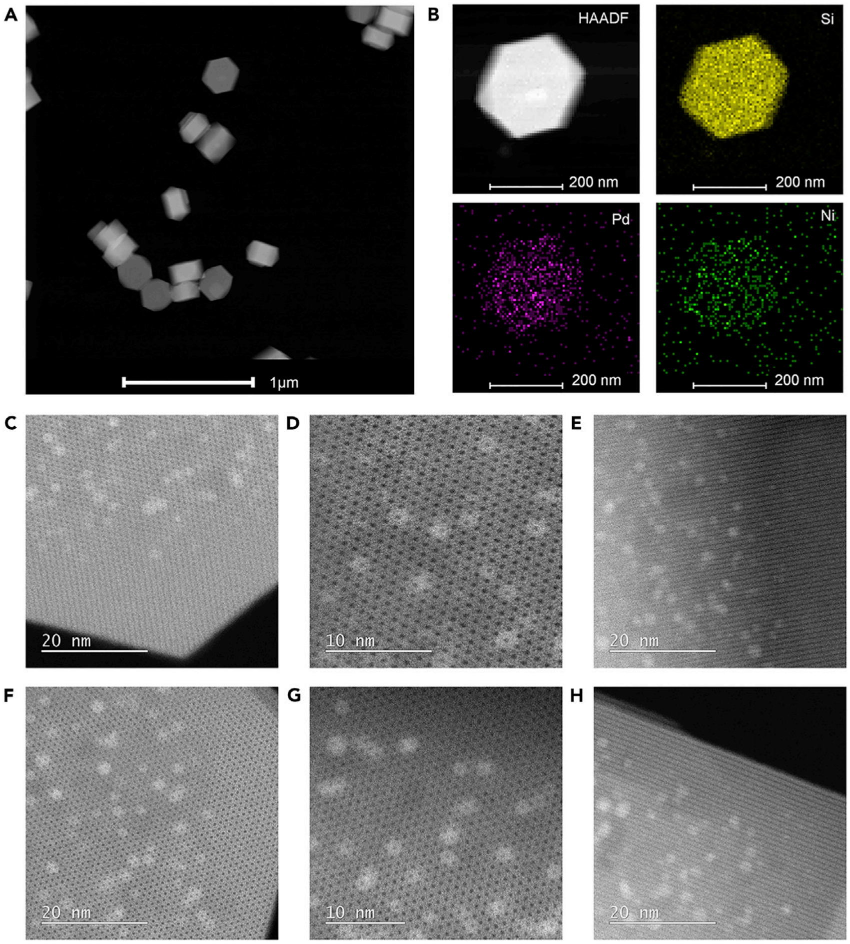

Figure 2. Elemental Mapping and Cs-Corrected STEM Images

(A and B) STEM image (A) and HAADF-STEM image (B) of 0.8Pd0.2Ni(OH)$_2$@S-1 catalyst and the corresponding EDX mapping images for Si, Pd, and Ni elements.

(C–E) Cs-corrected STEM images of 0.8Pd0.2Ni(OH)$_2$@S-1 catalyst viewed along b axis orientation with low magnification (C), viewed along b axis orientation with high magnification (D), and viewed along other orientation (E).

(F–H) Cs-corrected STEM images of Pd@S-1 catalyst viewed along b axis orientation with low magnification (F), viewed along b axis orientation with high magnification (G), and viewed along other orientation (H).

Scale bars represent 1 μm (A), 200 nm (B), 20 nm (C, E, F, and H), and 10 nm (D and G).

The element distribution of the 0.8Pd0.2Ni(OH)$_2$@S-1 sample was determined by STEM imaging, high-resolution high-angle annular dark-field (HAADF)-STEM imaging, and energy-dispersive X-ray (EDX) spectral mapping in Figures 2A and 2B. The Pd and Ni elements are uniformly located at nearly identical positions, indicating the formation of bimetallic clusters. The corresponding EDX spectrum further revealed the presence of Pd and Ni elements in the sample (Figure S7).

To further investigate the location of metal clusters in the zeolites, Cs-corrected HAADF-STEM was performed on 0.8Pd0.2Ni(OH)$_2$@S-1 (Figures 2C–2E) compared with Pd@S-1 (Figures 2F–2H). The images clearly reveal that the straight channels along the [010] direction are empty and intact, suggesting that the metal clusters might be located in the intersectional void spaces between the straight and sinusoidal channels of the **MFI** structure, in accordance with our previous work.[29] The

Please cite this article in press as: Sun et al., Subnanometric Hybrid Pd-M(OH)$_2$, M = Ni, Co, Clusters in Zeolites as Highly Efficient Nanocatalysts for Hydrogen Generation, Chem (2017), http://dx.doi.org/10.1016/j.chempr.2017.07.001

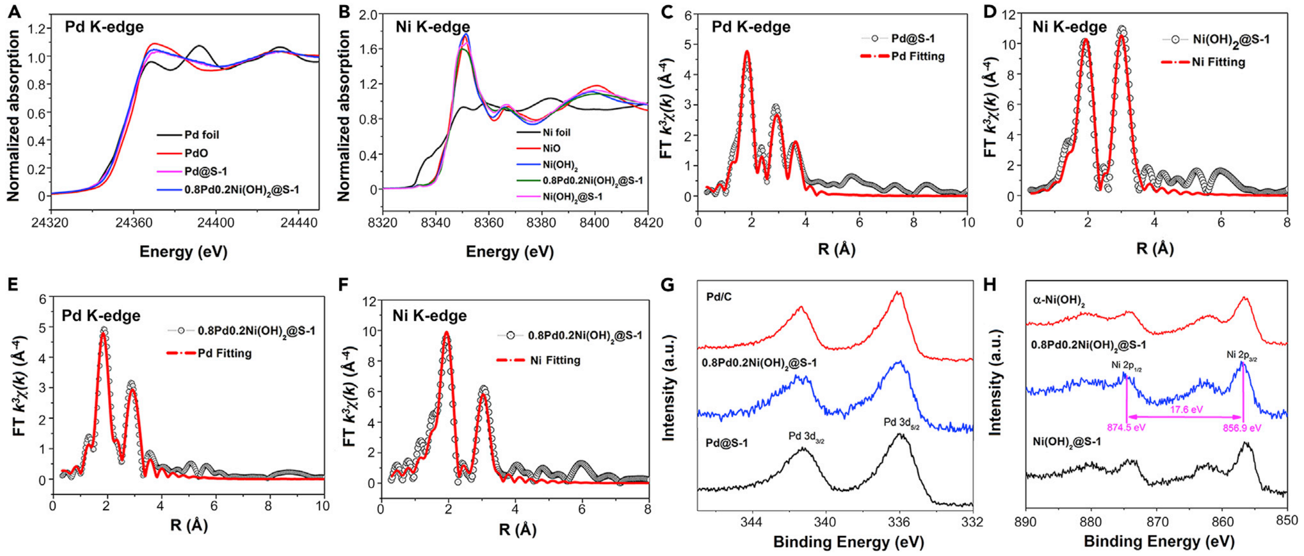

Figure 3. Characterization of Pd@S-1 and 0.8Pd0.2Ni(OH)$_2$@S-1 Catalysts Using XANES, EXAFS, and XPS Measurements

(A) Pd K-edge XANES spectra of Pd foil, PdO, Pd@S-1, and 0.8Pd0.2Ni(OH)$_2$@S-1 catalysts.

(B) Ni K-edge XANES spectra of Ni foil, NiO, Ni(OH)$_2$, and 0.8Pd0.2Ni(OH)$_2$@S-1 catalysts.

(C) Fourier transform of k^3-weighted EXAFS spectra of Pd@S-1 catalyst at Pd K-edge.

(D) Fourier transform of k^3-weighted EXAFS spectra of Ni(OH)$_2$@S-1 catalyst at Ni K-edge.

(E) Fourier transform of k^3-weighted EXAFS spectra of 0.8Pd0.2Ni(OH)$_2$@S-1 catalyst at Pd K-edge.

(F) Fourier transform of k^3-weighted EXAFS spectra of 0.8Pd0.2Ni(OH)$_2$@S-1 catalyst at Ni K-edge.

(G) Pd 3d XPS spectra of isolated metal samples after dissolving Pd@S-1 and 0.8Pd0.2Ni(OH)$_2$@S-1 catalysts in NaOH solution compared with commercial Pd/C catalyst.

(H) Ni 2p XPS spectra of dissolved 0.8Pd0.2Ni(OH)$_2$@S-1 and Ni(OH)$_2$@S-1samples compared with the α-Ni(OH)$_2$ sample.

brightness of the metal clusters displaced in Cs-corrected HAADF-STEM images appears different, indicating the different locations of metal clusters within the S-1 zeolite. Furthermore, all the metal-containing samples show almost the same ^{29}Si magic angle spinning nuclear magnetic resonance (NMR) spectra as that of pure S-1 zeolite (Figure S8), indicating that the zeolite framework remains intact after the metal clusters are confined in the micropore of zeolite.

To provide the local structure information of the zeolite-supported metal clusters, X-ray absorption near-edge structure (XANES) and EXAFS spectra of Pd@S-1, Ni(OH)$_2$@S-1, and 0.8Pd0.2Ni(OH)$_2$@S-1 samples were measured (Figures 3A–3F); and the structural parameters obtained from EXAFS fitting are summarized in Table S2. The Ni K-edge XANES spectra of Ni(OH)$_2$@S-1 and 0.8Pd0.2Ni(OH)$_2$@S-1 strongly resembled that of the Ni(OH)$_2$ reference spectrum, indicating the possible existence of Ni(OH)$_2$ species in these multi-metallic clusters. This is somewhat unusual, as Ni(OH)$_2$ typically transforms into NiO after calcination in air, and further converts to Ni metal after reduction under a H$_2$ atmosphere. The formation of Ni(OH)$_2$ species instead of Ni metal clusters in S-1 zeolite could be explained by the ability of the zeolite framework to stabilize ultrasmall Ni(OH)$_2$ species, preventing them from undergoing further dehydration and reduction to form Ni metal species. However, the Pd K-edge XANES spectra of Pd@S-1 and 0.8Pd0.2Ni(OH)$_2$@S-1 exhibited some differences from both Pd foil and PdO reference spectra. This can be attributed to the ultrasmall particle sizes and the strong interaction between Pd and the oxygen atoms of Ni(OH)$_2$ or even the zeolite framework itself, leading to an increased oxidation state for these Pd atoms.[15,37] Notably, a small shift of the Pd K-edge absorption to the lower binding energy for 0.8Pd0.2Ni(OH)$_2$@S-1 can be found compared with Pd@S-1, which demonstrates that the Pd atoms in 0.8Pd0.2Ni(OH)$_2$@S-1 might possess a higher electron density than that in Pd@S-1. In the Pd K-edge Fourier-transformed EXAFS spectrum of Pd@S-1, significant peaks were detected at ~1.97Å, ~2.74Å, and ~3.43Å; these peaks were identified as Pd–O, first shell Pd–Pd metallic bonds, and second shell Pd–Pd bonds from the Pd–O–Pd structure, respectively.[38] It is noteworthy that the Pd–O distance of 0.8Pd0.2Ni(OH)$_2$@S-1 (2.00 ± 0.01Å) was slightly longer than that of Pd@S-1 (1.97 ± 0.01Å). This also suggests a higher electron density for the Pd atoms in 0.8Pd0.2Ni(OH)$_2$@S-1 as a result of less charge transfer from Pd atoms to O atoms. In the Ni K-edge EXAFS spectra of Ni(OH)$_2$@S-1 and 0.8Pd0.2Ni(OH)$_2$@S-1, peaks of Ni–O (2.06 ± 0.01Å) and Ni–Ni (3.06 ± 0.01Å) bonds were observed; these bond lengths are consistent with those found in the Ni(OH)$_2$ reference spectrum (Figure S9).[12] Together, the above results demonstrate that these bimetallic clusters comprise a combination of Pd metal and Ni(OH)$_2$ species. Most significantly, it was observed that the average coordination numbers of the Pd–Pd metallic bonds in Pd@S-1 and 0.8Pd0.2Ni(OH)$_2$@S-1 are only 2.3 to 3.1 (Table S2), indicating that the bimetallic Pd-Ni(OH)$_2$ clusters possess ultrasmall subnanometric sizes.[39]

X-ray photoelectron spectroscopy (XPS) analyses were further used to characterize the elemental composition of bimetallic clusters (Figures 3G and 3H). No XPS signals were initially observed in the XPS spectrum of 0.8Pd0.2Ni(OH)$_2$@S-1 because the metal clusters were totally encapsulated within the zeolites. However, when 0.8Pd0.2Ni(OH)$_2$@S-1 was dissolved in NaOH solution, Pd3d$_{5/2}$ and Pd3d$_{3/2}$ peaks were observed at 336.0 eV and 341.3 eV, as well as Ni2p$_{3/2}$ and Ni2p$_{1/2}$ peaks at 856.9 eV and 874.5 eV. These peak positions correspond to the typical zero-valent Pd metal and divalent Ni(OH)$_2$ phases, respectively, as shown by their resemblance to peaks obtained from commercial Pd/C catalyst, dissolved Pd@S-1, dissolved Ni(OH)$_2$@S-1, and as-synthesized α-Ni(OH)$_2$ references.[40]

Stability Measurement

To investigate the stability of confined bimetallic Pd-Ni(OH)$_2$ clusters under commonly used industrial conditions, samples of 0.8Pd0.2Ni(OH)$_2$@S-1 were calcined under various oxidation-reduction atmospheres at 600°C–700°C as well as in the presence of water vapor at 600°C. As shown in Figures S10 and S11, the particle sizes of bimetallic Pd-Ni(OH)$_2$ clusters showed only a small increase of 0.2–0.3 nm after calcination at 700°C for 2 hr under a H_2 and N_2 atmosphere, respectively. After treatment under an O_2 atmosphere at 600°C, the average size of the metal clusters changed just slightly, increasing from 1.7 to 2.2 nm (Figure S12). Moreover, after aging treatments in water vapor at 600°C, the metal clusters of 0.8Pd0.2Ni(OH)$_2$@S-1 also retained their stability, with a slight increase from 1.7 to 2.2 nm. Even after increasing the flow of water vapor to 18 mL/min at 600°C, a metal cluster size of ~2.6 nm was still observed (Figure S13). In contrast to the stability of these bimetallic clusters, the metal particles deposited on the Pd/S-1-im and 0.8Pd0.2Ni(OH)$_2$/S-1-im samples using the impregnation method aggregated dramatically after calcination at 700°C for 2 hr under a N_2 atmosphere, resulting in increased particle sizes up to 5.3 and 6.3 nm, respectively. This further confirms that the confinement effect of zeolites can considerably improve the thermal stability of the encapsulated metal clusters. Notably, the samples of Pd@S-1 and 0.8Pd0.2Ni(OH)$_2$@S-1 also exhibited exceptional stability after 4-fold cycles of oxidation-reduction treatment at 650°C, showing just slightly increased particle sizes (by ~0.4 nm) (Figures S14 and S15). Furthermore, the crystal morphology, crystallinity, and metal loading amount of 0.8Pd0.2Ni(OH)$_2$ were nearly unchanged after treatment at high temperature (Figures S16–S21 and Table S3).

Please cite this article in press as: Sun et al., Subnanometric Hybrid Pd-M(OH)$_2$, M = Ni, Co, Clusters in Zeolites as Highly Efficient Nanocatalysts for Hydrogen Generation, Chem (2017), http://dx.doi.org/10.1016/j.chempr.2017.07.001

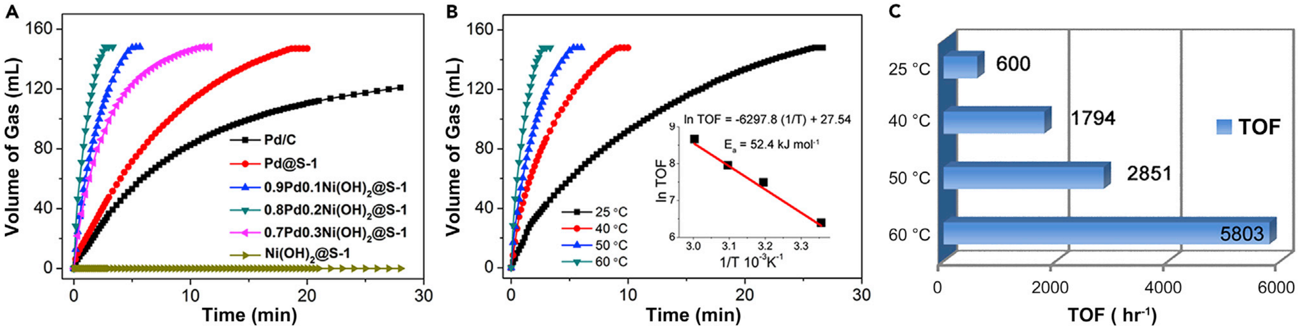

Figure 4. Catalytic Activity of Hydrogen Generation from Formic Acid Decomposition

(A) Volume of the released gas ($CO_2 + H_2$) versus time for the dehydrogenation of 2 M FA solution over Pd/C, Pd@S-1, Ni(OH)$_2$@S-1, and Pd-Ni(OH)$_2$@S-1 catalysts at 60°C (n_{metal}/n_{FA} = 0.012).

(B and C) Volume of the released gas ($CO_2 + H_2$) versus time (B) and corresponding initial TOF values (C) of H_2 generation for the decomposition of 2 M FA solution at different temperatures over 0.8Pd0.2Ni(OH)$_2$@S-1 catalyst. Inset of (B): Arrhenius plot (ln TOF versus 1/*T*).

Shape-Selective Catalytic Reaction

As an important high-value-added reaction, the shape-selective hydrogenation of nitrobenzene and 3-nitrotoluene with different molecular sizes was selected as the mode reaction over the 0.8Pd0.2Ni(OH)$_2$@S-1 and Pd/C catalysts. The commercial Pd/C catalyst showed complete conversion for the hydrogenation of both nitrobenzene and 3-nitrotoluene, independently of the molecule size of the substrate, which was confirmed by the UV/visible (UV/vis) absorption and gas chromatography-mass spectrometry (GC-MS) analyses in Figure S22. In the case of the 0.8Pd0.2Ni(OH)$_2$@S-1 catalyst, however, restricted access of the hydrogenation of 3-nitrotoluene into the micropores of the S-1 zeolite allowed only a negligible amount of conversion, despite complete conversion of nitrobenzene. These results demonstrate the excellent shape-selective catalytic activity of the zeolite-confined nanocatalysts.

Catalytic Activity of Hydrogen Generation from Formic Acid Decomposition

Catalytic activity of FA decomposition for hydrogen generation without any additive at 60°C and 25°C was investigated for the hybrid bimetallic Pd-Ni(OH)$_2$@S-1 catalysts compared with Pd@S-1 catalyst, Ni(OH)$_2$@S-1, and the commercial Pd/C catalyst (Figures 4A and S23). Compared with the Pd/C and monometallic Pd@S-1 catalysts, the Pd-Ni(OH)$_2$@S-1 catalysts exhibited considerably improved activity for the complete decomposition of FA. Notably, the 0.8Pd0.2Ni(OH)$_2$@S-1 catalyst showed the highest catalytic activity; 147 mL of CO-free (<10 ppm) gas could be released within 2.67 min at 60°C without any additive, reflecting the complete and efficient decomposition of FA into H_2 and CO_2. The formation of released gases was determined by GC analysis (Figures S24 and S25). In general, the Pd clusters with smaller particle size are prone to deactivation because of the adsorption of poisonous CO intermediates.[41] No detectable amount of CO (<10 ppm) was found in the gas mixture generated from the decomposition of FA over the 0.8Pd0.2Ni(OH)$_2$@S-1 catalyst, which ensures that the 0.8Pd0.2Ni(OH)$_2$@S-1 catalyst can retain excellent catalytic activity and avoid poisoning in the FA decomposition reaction. Significantly, the 0.8Pd0.2Ni(OH)$_2$@S-1 catalyst afforded an exceedingly high initial and total TOF values up to 5,803 hr^{-1} and 1,879 hr^{-1} at 60°C, which are more than a 14-fold and 9-fold improvement compared with the commercial Pd/C catalyst and monometallic Pd@S-1 catalyst, respectively. To the best of our knowledge, such TOF values represent the highest activity for heterogeneously catalyzed FA decomposition without additives and under similar conditions and even exceed most results obtained with additives (Table S4).[42–45] The initial

H_2 generation rate of the 0.8Pd0.2Ni(OH)$_2$@S-1 catalyst was calculated to be 1,418 L H_2 hr^{-1} g$_{metal}$$^{-1}$, corresponding to a theoretical power density of 1,915 W hr^{-1} g$_{metal}$$^{-1}$ for energy generation. Assuming an operation efficiency of 60%, 1.0 g of the 0.8Pd0.2Ni(OH)$_2$@S-1 catalyst would be adequate to supply H_2 for 4–14 small (0.5–2.0 Wh) proton exchange membrane fuel cell devices.[46]

It was observed that the monometallic Ni(OH)$_2$@S-1 catalyst itself showed no catalytic activity, and the physical mixture of Pd@S-1 and Ni(OH)$_2$@S-1 catalysts also exhibited activity identical to that of the monometallic Pd@S-1 catalyst (Figure S26). These results indicate that the bimetallic synergistic effect of Pd and Ni(OH)$_2$ clusters in zeolite plays an important role in improving the catalytic activity for the generation of H_2. Previous work has revealed that a more electron-rich Pd surface favors rate-determining C–H activation of the Pd-formate intermediate to produce H_2 and CO_2.[16] The electron-rich Pd surface of the 0.8Pd0.2Ni(OH)$_2$@S-1 catalyst as suggested by the EXAFS studies could be beneficial for enhancing its catalytic activity for FA decomposition.

On the other hand, the Pd@S-1/Ni(OH)$_2$-im catalysts synthesized by impregnating $Ni(NO_3)_2$ solution into Pd@S-1 catalysts exhibited improved H_2 generation activity relative to Pd@S-1, albeit still much lower than the *in situ*-synthesized 0.8Pd0.2Ni(OH)$_2$@S-1 catalyst (Figure S27). The hydrogen generation rates over catalysts synthesized using *in situ*-synthesized Pd or Pd-Ni(OH)$_2$ clusters encapsulated within S-1 zeolites were much higher than those of their counterparts synthesized using the impregnation method (Figure S28). The above results indicate that the ultrasmall Pd-Ni(OH)$_2$ clusters size is also crucial for its superior catalytic activity for the generation of H_2 from FA.

The H_2 generation rates were further enhanced with increase in the reaction temperature (Figures 4B, 4C, and S29). The apparent activation energy (E_a) of 0.8Pd0.2Ni(OH)$_2$@S-1 and Pd@S-1 catalysts was 52.4 kJ/mol and 58.9 kJ/mol, respectively; these values are lower than most of the reported values (Table S5).[36,47] Moreover, the decreased E_a value of 0.8Pd0.2Ni(OH)$_2$@S-1 compared with Pd@S-1 further helps to explain the higher catalytic activity of the hybrid bimetallic catalyst compared with the monometallic catalyst.

The recycling experiment with the 0.8Pd0.2Ni(OH)$_2$@S-1 catalyst for FA dehydrogenation showed that the catalytic activity after 10 cycles was identical to that over the fresh catalyst (Figure S30). Significantly, the 0.8Pd0.2Ni(OH)$_2$@S-1 catalyst showed no decay in activity after being stored under atmospheric conditions for 300 days (Figure S31). Moreover, the morphology, crystallinity, and the metal cluster size of recycled 0.8Pd0.2Ni(OH)$_2$@S-1 catalysts were almost the same as those of the fresh catalyst, demonstrating the superior recyclability of the 0.8Pd0.2Ni(OH)$_2$@S-1 catalyst during FA decomposition (Figures S32–S35).

The base and/or acid sites of zeolite can affect the catalytic activity for FA dehydrogenation. In our previous work, we found that the additionally introduced basic sites of zeolite that are beneficial for the cleavage of the O–H bonds in FA molecules can enhance the catalytic performance of FA dehydrogenation.[29] To further investigate the influence of acid sites of zeolite on FA decomposition, Al atoms were introduced into the zeolite framework, and the resultant aluminosilicate zeolites (ZSM-5, **MFI**), denoted as 0.8Pd0.2Ni(OH)$_2$@ZSM-5 catalysts (Si/Al = 200 and 100) with different acidities, were used for the reaction of FA decomposition at 60°C and compared with the 0.8Pd0.2Ni(OH)$_2$@S-1 catalyst. Measurement of temperature-programmed desorption of ammonia (NH_3-TPD) demonstrated that with the increase in Al content, the acidity of zeolite was increased (Figure S36). Compared with the 0.8Pd0.2Ni(OH)$_2$@S-1 catalyst, the catalytic activity of the 0.8Pd0.2Ni(OH)$_2$@ZSM-5 catalysts was remarkably reduced (Figure S37). Notably, the 0.8Pd0.2Ni(OH)$_2$@ZSM-5 (Si/Al = 100) catalyst with the highest acidity exhibited the worst catalytic performance among the three catalysts. Only 80 mL of gas (about 55% conversion of FA) could be finally released in 20 min, affording a lower initial TOF of 1,067 hr^{-1}, which was just about one fifth that of the 0.8Pd0.2Ni(OH)$_2$@S-1 catalyst (TOF = 5,803 hr^{-1}). The catalytic results reveal that the acidity of zeolite is not favorable for the dehydrogenation of FA.

Density Functional Theory Calculations of FA Decomposition

Because of the structural complexity of the bulk structure of this material, it is difficult to obtain structural information on the small Pd or Pd-Ni(OH)$_2$ clusters encapsulated within S-1 zeolites by experimental characterization. Theoretical studies based on first-principle calculations may offer an alternative to explore the metal-support interaction at the atomic level and provide some electronic information that cannot be easily obtained in experiments. Because the close-packed (111) facet was found to be the dominant facet in real supported palladium catalysts, in this work we chose the Pd(111) surface as the surface model of the Pd@S-1 catalyst. For the transition metal atom/clusters deposited on oxide/hydroxide supports, the model of a heterogeneous catalyst is adopted by a supported metal cluster on the oxide/hydroxide surfaces, which has been generally accepted for understanding the metal-support interaction in many theoretical studies.[48–51] Here, a periodic surface of Pd-Ni(OH)$_2$ was modeled by a two-layer Ni(OH)$_2$ (001) slab with a (5 × 5) unit cell and a three-layer Pd cluster containing 19 Pd atoms placed on this slab (Figure S38).

To account for the effect of the Pd-Ni(OH)$_2$ interface for the improved catalytic performance, the mechanism of FA decomposition on both Pd(111) and Pd-Ni(OH)$_2$ surfaces was studied by first-principle density functional theory (DFT) calculations, and the calculated potential energy profiles on both Pd(111) and Pd-Ni(OH)$_2$ surfaces are presented in Figure 5. More computational details are given in Supplemental Information. Based on the calculated results, FA adsorbs on the top site on Pd(111) with an adsorption energy of -55.0 kJ/mol, while it prefers to bind at the interface of the Pd$_{19}$-Ni(OH)$_2$ surface, with an adsorption energy of -77.2 kJ/mol. Seen from Figure 5A, FA decomposition proceeds via a three-step process on Pd(111) with a rate-determining energy barrier of 107.2 kJ/mol, which corresponds well with the results of previous reports.[52–54] While on the Pd-Ni(OH)$_2$ surface, the adsorbed FA molecule undergoes two successive dehydrogenation steps (Figure 5B) to form CO_2 and dissociatively adsorbed hydrogen. It is seen that the first dehydrogenation step to form HCOO is the rate-determining step for the FA decomposition process on the bimetallic surface. The rate-determining energy barrier of 58.9 kJ/mol is much lower than that on the Pd(111) surface. The theoretical calculations show that the FA decomposition is facilely achieved at the interface of the Pd-Ni(OH)$_2$ surface, and thus the bimetal Pd and Ni(OH)$_2$ catalyst exhibits enhanced catalytic activation for FA decomposition compared with the monometallic Pd catalyst.

Pd-Co(OH)$_2$@S-1 Catalysts for FA Decomposition

To further verify the active interfacial effect between Pd and transition metal hydroxide clusters, the Pd-Co(OH)$_2$@S-1 catalysts (Pd/Co(OH)$_2$ = 9/1 and 8/2) were also synthesized *in situ* by adding $[Co(NH_2CH_2CH_2NH_2)_3]^{2+}$ complex into the starting synthesis system. The resulting Pd-Co(OH)$_2$@S-1 catalysts showed similar metal loadings (0.64 wt %), bimetallic cluster size (Figure S39), and crystallinity (Figure S40)

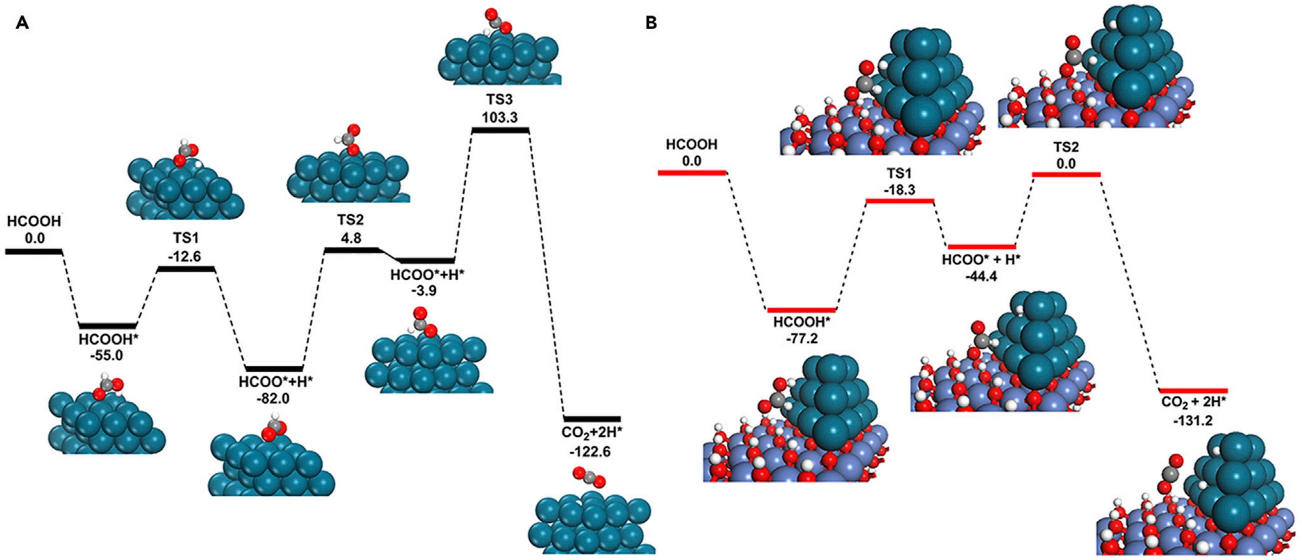

Figure 5. Potential Energy Diagrams and Optimized Geometries for All Reaction Intermediates and Transition States for FA Decomposition on the Pd and Pd-Ni(OH)$_2$ Surfaces

(A) Pure Pd(111) surface. TS, transition state.

(B) Pd-Ni(OH)$_2$ surface. Energies (kJ/mol) include zero-point-energy correction. Color scheme: white, H; red, O; gray, C; cyan, Pd; blue, Ni.

compared with the Pd-Ni(OH)$_2$@S-1 catalysts. XPS spectra showed the typical peaks of zero-valent Pd metal and divalent Co(OH)$_2$ phases (Figure S41). Most significantly, the Pd-Co(OH)$_2$@S-1 catalysts also exhibited a remarkably improved FA decomposition rate relative to Pd@S-1 and were comparable with the Pd-Ni(OH)$_2$@S-1 catalyst (Figure S42). These results further indicate that the synergistic effect between the interfaces of ultrasmall Pd and transition metal hydroxide clusters is responsible for enhancing the catalytic activity of these hybrid bimetallic nanocatalysts.

Conclusion

We have demonstrated a facile and one-pot synthesis strategy to prepare subnanometric non-noble metal hydroxide-containing hybrid bimetallic clusters encapsulated within nanosized purely siliceous silicalite-1 zeolite using metallic ethylenediamine complex mixtures as precursors via a hydrothermal synthesis method. The hybrid bimetallic nanocatalysts exhibit excellent shape-selective catalytic performance and highly efficient CO-free generation of H_2 via complete FA decomposition without any additives under mild conditions. Significantly, the 0.8Pd0.2Ni(OH)$_2$@S-1 catalyst affords an exceedingly high initial and total TOF values up to 5,803 hr^{-1} and 1,879 hr^{-1} at 60°C, which are among the highest values ever reported under similar conditions. EXAFS studies indicate that the Pd surface of the 0.8Pd0.2Ni(OH)$_2$@S-1 catalyst is electron-rich compared with the Pd@S-1 catalyst, which is beneficial for improving the catalytic activity of hybrid bimetallic catalysts. On the other hand, DFT calculations demonstrate that the interfacial effect between ultrasmall Pd and transition metal hydroxide clusters can considerably decrease the activation barrier for FA decomposition, thereby enhancing catalytic activity. The as-synthesized catalysts exhibit excellent stability after calcination in various industrial oxidation-reduction conditions at 600°C–700°C and recycling stability during FA decomposition because the bimetallic hybrid clusters are well confined within the zeolite matrix. The superb catalytic performance and excellent thermal and recycling stabilities of these hybrid bimetal nanocatalysts confined in zeolites not only promise their practical application for fuel cells using FA as an efficient medium for hydrogen storage

Please cite this article in press as: Sun et al., Subnanometric Hybrid Pd-M$(OH)_2$, M = Ni, Co, Clusters in Zeolites as Highly Efficient Nanocatalysts for Hydrogen Generation, Chem (2017), http://dx.doi.org/10.1016/j.chempr.2017.07.001

but also raise more possibilities for their use in other important high-performance catalytic reactions.

EXPERIMENTAL PROCEDURES

Chemicals and Materials

All chemicals and materials were obtained from commercial sources and used without further purification unless otherwise specified. Tetrapropylammonium hydroxide solution (TPAOH, 25 wt %), cobalt nitrate ($Co(NO_3)_2 \cdot 6H_2O$), and nitrobenzene were purchased from Sinopharm Chemical Reagent Co. Tetraethylorthosilicate (TEOS), nickel nitrate ($Ni(NO_3)_2 \cdot 6H_2O$), ethylenediamine ($NH_2CH_2CH_2NH_2$), sodium borohydride ($NaBH_4$), and aniline were purchased from Tianjin Fuchen Chemical Reagents Factory. Aluminum sulfate ($Al_2(SO_4)_3 \cdot 18H_2O$) was purchased from Guangfu Chemical Reagent Co. Palladium chloride ($PdCl_2$) was purchased from Shanghai Chemical Reagent Co. Urea ($CO(NH_2)_2$) was purchased from Xilong Chemical Co. 3-Nitrotoluene was purchased from Chengdu Kelong Chemical Reagent Factory. 3-Toluidine was purchased from Shanghai Macklin Biochemical Co. Dichloromethane (CH_2Cl_2) was purchased from Biaoshiqi Science and Technology Development Co. FA was purchased from Aladdin. Pd/C catalyst was obtained from a commercial Pd/C catalyst (loading 5 wt % Pd; Aladdin) followed by reduction in flowing H_2 with linear heating to 200°C for 2 hr and holding for 2 hr.

Synthesis of $[Pd(NH_2CH_2CH_2NH_2)_2]Cl_2$, $[Ni(NH_2CH_2CH_2NH_2)_3](NO_3)_2$, and $[Co(NH_2CH_2CH_2NH_2)_3](NO_3)_2$ Solutions

The solution of $[Pd(NH_2CH_2CH_2NH_2)_2]Cl_2$ was prepared by mixing 0.32 g of $PdCl_2$ in 10 mL of aqueous solution containing 2 mL of ethylenediamine under stirring at room temperature until complete dissolution. The solution of $[Ni(NH_2CH_2CH_2NH_2)_3](NO_3)_2$ or $[Co(NH_2CH_2CH_2NH_2)_3](NO_3)_2$ was prepared by mixing 0.95 g of $Ni(NO_3)_2 \cdot 6H_2O$ or $Co(NO_3)_2 \cdot 6H_2O$ into 10 mL of aqueous solution containing 2 mL of ethylenediamine under stirring at room temperature until complete dissolution.

Synthesis of Pd@S-1 and $Ni(OH)_2$@S-1 Catalysts

Pd@S-1 catalyst was synthesized with a molar composition of TEOS:TPAOH:H_2O:$[Pd(NH_2CH_2CH_2NH_2)_2]Cl_2$ of 1:0.4:35:0.0045 under hydrothermal conditions at 170°C for 4 days as described in our previous work.[29] The as-synthesized solid product was calcined in air at 550°C for 8 hr to remove templates, followed by reduction in a flowing H_2 atmosphere (linear heating to 400°C for 2 hr and holding for 2 hr). Similarly, the $Ni(OH)_2$@S-1 catalyst was synthesized with a similar synthesis procedure as the Pd@S-1 catalyst, except a suitable amount of $[Ni(NH_2CH_2CH_2NH_2)_3](NO_3)_2$ solution was added instead of $[Pd(NH_2CH_2CH_2NH_2)_2]Cl_2$ solution. After calcination in air at 550°C for 8 hr, the catalyst was reduced in flowing H_2 with linear heating to 400°C for 2 hr and holding for 2 hr, followed by heating to 500°C for 30 min and holding for 1 hr. The molar quantities of Pd and Ni were kept the same for the Pd@S-1 and $Ni(OH)_2$@S-1 catalysts.

Synthesis of xPd$(1-x)$Ni$(OH)_2$@S-1 (x = 0.9, 0.8, and 0.7) and yPd$(1-y)$Co$(OH)_2$@S-1 (y = 0.9 and 0.8) Catalysts

xPd$(1-x)$Ni$(OH)_2$@S-1 catalysts were synthesized in gels with molar compositions of TEOS:TPAOH:H_2O:$[Pd(NH_2CH_2CH_2NH_2)_2]^{2+}$: $[Ni(NH_2CH_2CH_2NH_2)_3]^{2+}$ of 1:0.4:35:a:b (a:b = 9:1, 8:2, or 7:3) under similar conditions as for the synthesis of the Pd@S-1 catalyst, except that suitable amounts of both $[Pd(NH_2CH_2CH_2NH_2)_2]Cl_2$ and $[Ni(NH_2CH_2CH_2NH_2)_3](NO_3)_2$ solutions (0.942 mL and 0.058 mL, 0.88 mL and 0.12 mL, 0.81 mL and 0.19 mL) were added to the reaction mixtures, resulting in molar ratios $n_{Pd}/(n_{Pd} + n_{Ni})$ equal to 0.9, 0.8, and 0.7, respectively. The metal content of $(m_{Pd} + m_{Ni})/m_{SiO_2}$ was kept at a constant 0.008. After calcination in air at 550°C for 8 hr, the catalysts were reduced in flowing H_2 with linear heating to 400°C for 2 hr and holding for 2 hr, followed by heating to 500°C for 30 min and holding for 1 hr. Similarly, yPd(1 − y)Co(OH)$_2$@S-1 catalysts were also synthesized with synthetic procedures similar to that for the Pd@S-1 catalyst, except suitable amounts of $[Co(NH_2CH_2CH_2NH_2)_3](NO_3)_2$ and $[Pd(NH_2CH_2CH_2NH_2)_2]Cl_2$ solutions were added to the synthesis gels before adding TEOS.

Synthesis of 0.8Pd0.2Ni(OH)$_2$@ZSM-5 Catalysts

The synthetic process for the 0.8Pd0.2Ni(OH)$_2$@ZSM-5 catalysts was similar to that for the 0.8Pd0.2Ni(OH)$_2$@S-1 catalyst, except for the introduction of some of $Al_2(SO_4)_3$ into the synthesis gel, and the molar ratios of Si/Al were 200 and 100, respectively.

Preparation of Pd@S-1/xNi(OH)$_2$-im Catalysts

Pd@S-1/xNi(OH)$_2$-im catalysts were prepared by impregnating $Ni(NO_3)_2$ solution into Pd@S-1 samples. Typically, 0.7 g of reduced Pd@S-1 catalyst was impregnated with 0.17 mL of $Ni(NO_3)_2 \cdot 6H_2O$ solution (0.028 M, 0.062 M, and 0.106 M), affording molar ratios of $n_{Pd}/(n_{Pd} + n_{Ni})$ of 0.9, 0.8, and 0.7, respectively. The resulting solids were dried at 80°C in the oven overnight. Finally, the catalysts were reduced in flowing H_2 with linear heating to 400°C for 2 hr and holding for 2 hr, and then heating to 500°C for 30 min and holding for 1 hr.

Preparation of Pd/S-1-im and 0.8Pd0.2Ni(OH)$_2$/S-1-im Catalysts

The silicalite-1 zeolite support was synthesized with a molar composition of TEOS:TPAOH:H_2O of 1:0.4:35 as described in our previous work.[29] The Pd/S-1-im and 0.8Pd0.2Ni(OH)$_2$/S-1-im catalysts were prepared by the incipient wetness impregnation method with $(NH_4)_2PdCl_4$ and $Ni(NO_3)_2$ solution. To prepare the Pd/S-1-im catalyst, 1 g of calcined silicalite-1 zeolite was impregnated with a $(NH_4)_2PdCl_4$ solution. The solid obtained was dried at 80°C and then treated in flowing H_2 following the same procedure as used for Pd@S-1. The 0.8Pd0.2Ni(OH)$_2$/S-1-im catalyst was prepared by the same procedure as for the Pd/S-1-im catalyst except that the zeolite was impregnated with 0.23 mL of mixed solution containing $(NH_4)_2PdCl_4$ (0.224 M) and $Ni(NO_3)_2$ (0.056 M). The 0.8Pd0.2Ni(OH)$_2$/S-1-im catalyst was reduced in flowing H_2 with linear heating to 400°C for 2 hr and holding for 2 hr, and then heating to 500°C for 30 min and holding for 1 hr.

Synthesis of α-Ni(OH)$_2$ Sample

The α-Ni(OH)$_2$ sample was synthesized with a molar composition of 1.0 $Ni(NO_3)_2$:2.0 $CO(NH_2)_2$:2228 H_2O under conventional hydrothermal conditions at 100°C for 20 hr. Typically, 0.291 g of $Ni(NO_3)_2 \cdot 6H_2O$ was dissolved in 40 mL of deionized water under continuous stirring at room temperature. Urea (0.12 g) was then added into the above mixture, followed by continuous stirring for 5 min. Finally, the solution was then transferred into a 100 mL Teflon-lined stainless steel autoclave, and the crystallization was conducted in a conventional oven at 100°C for 20 hr under static conditions. The resultant solid product was centrifuged, washed with water and ethanol several times, and then dried at 60°C in the oven overnight. The phase of this α-Ni(OH)$_2$ was identified using powder X-ray diffraction (PXRD) (Figure S43).

Characterizations

PXRD patterns were recorded on a Rigaku D/Max 2550 diffractometer at 50 kV and 200 mA (Cu Kα radiation). The SEM images were measured with a Hitachi SU-8020 scanning electron microscope. The TEM images and corresponding EDX spectra were acquired using an FEI Tecnai G2 F20 electron microscope. Cs-corrected HAADF-STEM images were taken at 200 kV on a JEM-ARM200F scanning transmission electron microscope. The metal content in the zeolite samples was analyzed by a PerkinElmer Optima 3300 DV ICP-AES instrument. ^{29}Si MAS NMR measurements were made on a Varian Infinity Plus 400WB spectrometer with a resonance frequency of 79.5 MHz. N_2 adsorption/desorption measurements were performed on a Micromeritics ASAP 2020 analyzer at 77.35 K. Before starting the N_2 adsorption measurements, all the samples were activated by degassing *in situ* at about 623 K for 10 hr. XPS was conducted on a Thermo ESCALAB 250 spectrometer on separated metal species after dissolving Pd@S-1, 0.8Pd0.2Ni(OH)$_2$@S-1, 0.8Pd0.2Co(OH)$_2$@S-1, and Ni(OH)$_2$@S-1 samples in NaOH solution. The NH_3-TPD experiments were performed using a Micromeritics AutoChem II 2920 chemisorption analyzer. The XAFS spectra measurements at the Ni K-edge (E_0 = 8333 eV) and Pd K-edge (E_0 = 24,350 eV) were performed at beamline BL14W1 of the Shanghai Synchrotron Radiation Facility (SSRF) operated at 3.5 GeV under "top-up" mode with a constant current of 240 mA.[55] The XAFS data were recorded in transmission mode using high-flux ion chambers for the Ni K-edge and under fluorescence mode with standard Lytle ion chambers for the Pd K-edge. The energy was calibrated according to the absorption edge of a pure Ni or Pd foil, as appropriate. Athena and Artemis software were used to extract and fit the data. For the XANES part, the experimental absorption coefficients as a function of energy $\mu(E)$ were processed by background subtraction and normalization procedures, and reported as "normalized absorption." Based on the normalized XANES profiles, the oxidation state of nickel and palladium can be determined by comparison with the corresponding standards (NiO/Ni foil for Ni^{2+}/Ni^0 and PdO/Pd foil for Pd^{2+}/Pd^0). For the EXAFS data, the Fourier-transformed data in R space were analyzed by applying a first shell approximation for the Ni–O/Pd–O and a metallic Pd model for the Pd–Pd shells. The passive electron factors, $S_0{}^2$, were determined by fitting the experimental Ni or Pd foil data and fixing the Ni–Ni or Pd–Pd coordination number (CN) to be 12, and then fixed for further analysis of the measured samples. The parameters describing the electronic properties (e.g., correction to the photoelectron energy origin, E_0) and local structure environment, including CN, bond distance (R), and Debye-Waller factor, around the absorbing atoms were allowed to vary during the fitting process. The k^3 weighted fitted ranges for the k space were 3–12 (Ni) and 3–11 (Pd) $Å^{-1}$, and the fitting range for R spaces was selected to be 1–4 Å.

Thermal Stability Tests of Catalysts

The representative 0.8Pd0.2Ni(OH)$_2$@S-1 catalyst (0.1 g) was calcined in a 40 mL/min N_2 atmosphere at 700°C (linear heating to 700°C for 2 hr and holding for 2 hr). For comparison, the Pd@S-1/0.2Ni(OH)$_2$-im, Pd@S-1/0.3Ni(OH)$_2$-im, and 0.8Pd0.2Ni(OH)$_2$/S-1-im catalysts synthesized using the impregnation method were also treated under the same conditions. The 0.8Pd0.2Ni(OH)$_2$@S-1 catalysts were also calcined in a flowing O_2 and H_2 atmosphere (40 mL/min) at 500°C–700°C. The high-temperature oxidation-reduction cyclic treatment was performed on the Pd@S-1 and 0.8Pd0.2Ni(OH)$_2$@S-1 catalysts. Typically, the catalyst was first subjected to an oxidation treatment at 650°C in air with linear heating to 650°C for 2 hr and holding for 2 hr. After the oxidation treatment, the sample was then reduced at 650°C in H_2 with linear heating to 650°C for 2 hr and holding for 2 hr. The above reduction and oxidation treatment was considered as one cycle. Subsequently, the catalyst was further applied in three consecutive oxidation-reduction cycles. The 0.8Pd0.2Ni(OH)$_2$@S-1 catalyst was also treated at 500°C and 600°C for 5 hr with water vapor flow of 3 mL/min and 18 mL/min, respectively.

Please cite this article in press as: Sun et al., Subnanometric Hybrid Pd-M(OH)$_2$, M = Ni, Co, Clusters in Zeolites as Highly Efficient Nanocatalysts for Hydrogen Generation, Chem (2017), http://dx.doi.org/10.1016/j.chempr.2017.07.001

Reduction Reaction of Nitrobenzene and 3-Nitrotoluene

First, a mixture of 0.1 mL of $NaBH_4$ solution (438 mM) and 10 mL of nitrobenzene or 3-nitrotoluene substrate solution (1.46 mM) was added into a 25 mL round-bottomed flask. Next, 20.1 mg of 0.8Pd0.2Ni(OH)$_2$@S-1 catalyst or 2.2 mg of Pd/C catalyst with the same Pd content was added to the above mixture, and the molar ratio of $n_{Pd}/n_{substrate}$ was 0.07. The reduction reaction was performed at 25°C under continuous stirring for 5 min. After the reaction, the reactants and products were analyzed by UV/vis measurements. After extraction with dichloromethane, the reactants and products were further analyzed using a Thermo Fisher Trace ISQ GC-MS equipped with a TG-5MS column (60 m × 320 μm × 25 μm).

Catalytic Activity of Hydrogen Generation from Formic Acid Decomposition

The decomposition reaction of FA was carried out using an apparatus containing a reaction unit and a gas collecting device. Typically, a mixture of a suitable amount of catalyst and distilled water (1 mL) was first added in a 25 mL two-necked flask placed in a water bath with magnetic stirring (600 rpm) at temperatures of 25°C–60°C under an ambient atmosphere. The volume of released gas was measured using a gas burette and an electronic balance continuously recording the weight of excurrent water. FA (0.5 mL, 6.0 M) aqueous solution was injected into the flask using a syringe to initiate the reaction. The molar ratios of n_{metal}/n_{FA} were fixed at 0.012 for all the catalytic reactions. The collected gas products were analyzed using an Agilent GC 6890N instrument equipped with a thermal conductivity detector and Plot-Q column (Agilent J&W GC Columns, HP-PLOT/Q 19095P-Q04, 30 m × 530 μm × 40 μm). Further analyses for CO were performed on a GC-7900 gas chromatograph using a flame ionization detector (FID)-methanator (detection limit, ~10 ppm).

Durability Test of Catalysts for FA Decomposition

The catalyst isolated after the initial FA decomposition experiment was reused in the catalytic dehydrogenation of FA (0.5 mL, 6.0 M) at 60°C. These catalysts were isolated and reused for up to 10 consecutive catalytic cycles. Moreover, catalytic dehydrogenation of FA was also performed for the 0.8Pd0.2Ni(OH)$_2$@S-1 catalyst stored under atmospheric conditions for 300 days.

The Calculation of Turnover Frequency and H_2 Generation Rate (R_{H_2})

The initial TOF ($TOF_{Initial}$) and total TOF (TOF_{Total}) were calculated based on the quantity of metal atoms (Pd + Ni) in the catalysts when the conversion of FA reached up to 20% and 100%, respectively. The following equations were used:

$$TOF_{Initial} = \frac{PV_{Initial\ gas}/RT}{2\ n_{Metal} t_{Initial}}, \quad \text{(Equation 1)}$$

$$TOF_{Total} = \frac{PV_{Total\ gas}/RT}{2\ n_{Metal} t_{Total}}, \quad \text{(Equation 2)}$$

where P = 101.325 kPa; $V_{Initial\ gas}$ and $V_{Total\ gas}$ are the initial and total volume of released gas (H_2 and CO_2), corresponding to conversions of 20% and 100% toward the conversion of FA, respectively; $R = 8.3145\ m^3\ Pa\ mol^{-1}\ K^{-1}$; T = 298 K; n_{Metal} is the total molar number of metal atoms (Pd + Ni) in the catalyst; $t_{Initial}$ and t_{Total} are the time of the reaction in hours, corresponding to 20% and 100% conversion toward the decomposition of FA.

The H_2 generation rate (R_{H_2}) was calculated from the following equation:

$$R_{H_2} = \frac{V_{H_2}}{m_{Metal}\,t}, \quad \text{(Equation 3)}$$

Please cite this article in press as: Sun et al., Subnanometric Hybrid Pd-M(OH)$_2$, M = Ni, Co, Clusters in Zeolites as Highly Efficient Nanocatalysts for Hydrogen Generation, Chem (2017), http://dx.doi.org/10.1016/j.chempr.2017.07.001

where V_{H_2} is the initial volume of released gas (H_2 and CO_2), corresponding to the conversion of 20% toward the conversion of FA; m_{Metal} is the mass of metal atoms (Pd + Ni); t is the reaction time in hours, corresponding to the conversion of 20% toward the conversion of FA.

DFT Computational Methods

First-principle spin-polarized DFT calculations were performed using the Vienna ab initio Simulation Package.[56] The projector augmented wave pseudopotentials[57,58] were used to describe the electron-ion interactions. The exchange-correlation effects were treated by the Perdew-Burke-Ernzerhof functional[59] with the generalized gradient approximation. The energy cutoff for the plane-wave basis sets was set at 400 eV in all calculations.

The surface model of Pd-Ni(OH)$_2$ was constructed using periodic boundary conditions based on optimized Pd and Ni(OH)$_2$ bulk structures. A (5 × 5) supercell of Ni(OH)$_2$ (001) slab model with two layers was adopted as the support, and a three-layer Pd cluster containing 19 atoms with the exposed (111) surface facet was placed on top of the Ni(OH)$_2$ surface (Figure S38). In the optimization of the Pd-Ni(OH)$_2$ slab model, the Pd cluster and the upper layer of Ni(OH)$_2$ were allowed to fully relax, and the bottom layer of Ni(OH)$_2$ was fixed at the optimized bulk geometry. A vacuum region of 20 Å was used to remove any interactions between the periodic slabs. The slab model of the Pd(111) surface was built with a (3 × 3) supercell and five layers. The upper three layers of Pd(111) were relaxed, and the bottom two layers were fixed at the bulk geometry in structure optimization. The Brillouin zones were sampled with Monkhorst-Pack k points of 7 × 7 × 7 for bulk calculations and 3 × 3 × 1 for surface calculations. The geometry optimization was stopped until the force on each atom was less than 0.02 eV/Å. The transition states were located with the climbing-image nudged elastic band method and were verified by vibrational analysis. The energy barriers were calculated as the energy difference between the transition state and the reactants. The adsorption energy (E_{ads}) for the adsorbate was defined as

$$E_{ads} = E_{adsorbate\text{-}surface} - E_{surface} - E_{adsorbate}, \qquad \text{(Equation 4)}$$

where $E_{adsorbate}$, $E_{surface}$, and $E_{adsorbate\text{-}surface}$ represent the energies of the adsorbate in gas phase, the corresponding clean surface model, and the surface with the adsorbate, respectively.

SUPPLEMENTAL INFORMATION

Supplemental Information includes 43 figures and 5 tables and can be found with this article online at http://dx.doi.org/10.1016/j.chempr.2017.07.001.

AUTHOR CONTRIBUTIONS

J.Y. designed and supervised the project. Q.S. and N.W. contributed equally to this work, and carried out the synthesis, characterization, and the catalytic measurements. Q.S. wrote the manuscript, and J.Y. revised the manuscript. Q.B. and J.L. performed the theoretical calculations. R.S. and P.Z. performed EXAFS measurements of the samples and analyzed the results. R.B. and M.J. collaborated in characterizing the samples.

ACKNOWLEDGMENTS

The authors thank the Nation Key Research and Development Program of China (grant no. 2016YFB0701100), National Natural Science Foundation of China (grant nos. 21320102001, 21621001, 21373098, and 21373259) , and the National 111 Project (B17020) for supporting this work. The authors also thank Dr. Paul Duchesne (Department of Chemistry, Dalhousie University) for his kind help with revising the manuscript.

Received: March 14, 2017
Revised: April 19, 2017
Accepted: July 3, 2017
Published: August 31, 2017

REFERENCES AND NOTES

1. Gates, B.C. (1995). Supported metal clusters: synthesis, structure, and catalysis. Chem. Rev. *95*, 511–522.
2. Flytzani-Stephanopoulos, M., and Gates, B.C. (2012). Atomically dispersed supported metal catalysts. Annu. Rev. Chem. Biomol. Eng. *3*, 545–574.
3. Munnik, P., de Jongh, P.E., and de Jong, K.P. (2015). Recent developments in the synthesis of supported catalysts. Chem. Rev. *115*, 6687–6718.
4. Flytzani-Stephanopoulos, M. (2014). Gold atoms stabilized on various supports catalyze the water–gas shift reaction. Acc. Chem. Res. *47*, 783–792.
5. Lu, J., Fu, B., Kung, M.C., Xiao, G., Elam, J.W., Kung, H.H., and Stair, P.C. (2012). Coking- and sintering-resistant palladium catalysts achieved through atomic layer deposition. Science *335*, 1205–1208.
6. Yang, X.-F., Wang, A., Qiao, B., Li, J., Liu, J., and Zhang, T. (2013). Single-atom catalysts: a new frontier in heterogeneous catalysis. Acc. Chem. Res. *46*, 1740–1748.
7. Vajda, S., Pellin, M.J., Greeley, J.P., Marshall, C.L., Curtiss, L.A., Ballentine, G.A., Elam, J.W., Catillon-Mucherie, S., Redfern, P.C., Mehmood, F., et al. (2009). Subnanometre platinum clusters as highly active and selective catalysts for the oxidative dehydrogenation of propane. Nat. Mater. *8*, 213–216.
8. Liu, L., Díaz, U., Arenal, R., Agostini, G., Concepción, P., and Corma, A. (2017). Generation of subnanometric platinum with high stability during transformation of a 2D zeolite into 3D. Nat. Mater. *16*, 132–138.
9. Liu, P., Zhao, Y., Qin, R., Mo, S., Chen, G., Gu, L., Chevrier, D.M., Zhang, P., Guo, Q., Zang, D., et al. (2016). Photochemical route for synthesizing atomically dispersed palladium catalysts. Science *352*, 797–800.
10. Qiao, B., Wang, A., Yang, X., Allard, L.F., Jiang, Z., Cui, Y., Liu, J., Li, J., and Zhang, T. (2011). Single-atom catalysis of CO oxidation using Pt_1/FeO_x. Nat. Chem. *3*, 634–641.
11. Guo, X., Fang, G., Li, G., Ma, H., Fan, H., Yu, L., Ma, C., Wu, X., Deng, D., Wei, M., et al. (2014). Direct, nonoxidative conversion of methane to ethylene, aromatics, and hydrogen. Science *344*, 616–619.
12. Chen, G., Zhao, Y., Fu, G., Duchesne, P.N., Gu, L., Zheng, Y., Weng, X., Chen, M., Zhang, P., Pao, C.-W., et al. (2014). Interfacial effects in iron-nickel hydroxide–platinum nanoparticles enhance catalytic oxidation. Science *344*, 495–499.
13. Subbaraman, R., Tripkovic, D., Strmcnik, D., Chang, K.-C., Uchimura, M., Paulikas, A.P., Stamenkovic, V., and Markovic, N.M. (2011). Enhancing hydrogen evolution activity in water splitting by tailoring Li^+-$Ni(OH)_2$-Pt interfaces. Science *334*, 1256–1260.
14. Subbaraman, R., Tripkovic, D., Chang, K.-C., Strmcnik, D., Paulikas, A.P., Hirunsit, P., Chan, M., Greeley, J., Stamenkovic, V., and Markovic, N.M. (2012). Trends in activity for the water electrolyser reactions on 3*d* M(Ni,Co,Fe,Mn) hydr(oxy)oxide catalysts. Nat. Mater. *11*, 550–557.
15. Huang, W., Wang, H., Zhou, J., Wang, J., Duchesne, P.N., Muir, D., Zhang, P., Han, N., Zhao, F., Zeng, M., et al. (2015). Highly active and durable methanol oxidation electrocatalyst based on the synergy of platinum-nickel hydroxide-graphene. Nat. Commun. *6*, 10035.
16. Yan, J.-M., Wang, Z.-L., Gu, L., Li, S.-J., Wang, H.-L., Zheng, W.-T., and Jiang, Q. (2015). AuPd-MnO_x/MOF-graphene: an efficient catalyst for hydrogen production from formic acid at room temperature. Adv. Energy Mater *5*, 4502–4505.
17. Čejka, J., Corma, A., and Zones, S.I. (2010). Zeolites and Catalysis: Synthesis, Reactions and Applications (Wiley-VCH Weinheim).
18. Corma, A. (1997). From microporous to mesoporous molecular sieve materials and their use in catalysis. Chem. Rev. *97*, 2373–2420.
19. Farrusseng, D., and Tuel, A. (2016). Perspectives on zeolite-encapsulated metal nanoparticles and their applications in catalysis. New J. Chem. *40*, 3933–3949.
20. Fenwick, O., Coutiño-Gonzalez, E., Grandjean, D., Baekelant, W., Richard, F., Bonacchi, S., De Vos, D., Lievens, P., Roeffaers, M., Hofkens, J., et al. (2016). Tuning the energetics and tailoring the optical properties of silver clusters confined in zeolites. Nat. Mater. *15*, 1017–1022.
21. Yang, M., Li, S., Wang, Y., Herron, J.A., Xu, Y., Allard, L.F., Lee, S., Huang, J., Mavrikakis, M., and Flytzani-Stephanopoulos, M. (2014). Catalytically active Au-$O(OH)_x^-$ species stabilized by alkali ions on zeolites and mesoporous oxides. Science *346*, 1498–1501.
22. Guzman, J., and Gates, B.C. (2003). Supported molecular catalysts: metal complexes and clusters on oxides and zeolites. Dalton Trans. *17*, 3303–3318.
23. Choi, M., Wu, Z., and Iglesia, E. (2010). Mercaptosilane-assisted synthesis of metal clusters within zeolites and catalytic consequences of encapsulation. J. Am. Chem. Soc. *132*, 9129–9137.
24. Goel, S., Wu, Z., Zones, S.I., and Iglesia, E. (2012). Synthesis and catalytic properties of metal clusters encapsulated within small-pore (SOD, GIS, ANA) zeolites. J. Am. Chem. Soc. *134*, 17688–17695.
25. Goel, S., Zones, S.I., and Iglesia, E. (2014). Encapsulation of metal clusters within MFI via interzeolite transformations and direct hydrothermal syntheses and catalytic consequences of their confinement. J. Am. Chem. Soc. *136*, 15280–15290.
26. Otto, T., Ramallo-López, J.M., Giovanetti, L.J., Requejo, F.G., Zones, S.I., and Iglesia, E. (2016). Synthesis of stable monodisperse AuPd, AuPt, and PdPt bimetallic clusters encapsulated within LTA-zeolites. J. Catal. *342*, 125–137.
27. Otto, T., Zones, S.I., and Iglesia, E. (2016). Challenges and strategies in the encapsulation and stabilization of monodisperse Au clusters within zeolites. J. Catal. *339*, 195–208.
28. de Jong, K.P., and Zečević, J. (2017). Porous catalysts: the platinum rush. Nat. Mater. *16*, 7–8.
29. Wang, N., Sun, Q., Bai, R., Li, X., Guo, G., and Yu, J. (2016). In situ confinement of ultrasmall Pd clusters within nanosized silicalite-1 zeolite for highly efficient catalysis of hydrogen generation. J. Am. Chem. Soc. *138*, 7484–7487.
30. Dai, C., Zhang, A., Liu, M., Gu, L., Guo, X., and Song, C. (2016). Hollow alveolus-like nanovesicle assembly with metal-encapsulated hollow zeolite nanocrystals. ACS Nano *10*, 7401–7408.
31. Dai, C., Zhang, A., Liu, M., Guo, X., and Song, C. (2015). Hollow ZSM-5 with silicon-rich surface, double shells, and functionalized interior with metallic nanoparticles and carbon nanotubes. Adv. Funct. Mater. *25*, 7479–7487.
32. Dai, C., Zhang, S., Zhang, A., Song, C., Shi, C., and Guo, X. (2015). Hollow zeolite encapsulated Ni-Pt bimetals for sintering and coking resistant dry reforming of methane. J. Mater. Chem. A. *3*, 16461–16468.
33. Dai, C., Li, X., Zhang, A., Liu, C., Song, C., and Guo, X. (2015). Pd and Pd-CuO nanoparticles in hollow silicalite-1 single crystals for enhancing selectivity and activity for the Suzuki-Miyaura reaction. RSC Adv. *5*, 40297–40302.

Please cite this article in press as: Sun et al., Subnanometric Hybrid Pd-M$(OH)_2$, M = Ni, Co, Clusters in Zeolites as Highly Efficient Nanocatalysts for Hydrogen Generation, Chem (2017), http://dx.doi.org/10.1016/j.chempr.2017.07.001

34. Chen, Y., Zhu, Q.-L., Tsumori, N., and Xu, Q. (2015). Immobilizing highly catalytically active noble metal nanoparticles on reduced graphene oxide: a non-noble metal sacrificial approach. J. Am. Chem. Soc. *137*, 106–109.

35. Dai, H., Xia, B., Wen, L., Du, C., Su, J., Luo, W., and Cheng, G. (2015). Synergistic catalysis of AgPd@ZIF-8 on dehydrogenation of formic acid. Appl. Catal. B Environ. *165*, 57–62.

36. Liu, Q., Yang, X., Huang, Y., Xu, S., Su, X., Pan, X., Xu, J., Wang, A., Liang, C., Wang, X., et al. (2015). A Schiff base modified gold catalyst for green and efficient H_2 production from formic acid. Energy Environ. Sci. *8*, 3204–3207.

37. Yan, H., Cheng, H., Yi, H., Lin, Y., Yao, T., Wang, C., Li, J., Wei, S., and Lu, J. (2015). Single-atom Pd1/graphene catalyst achieved by atomic layer deposition: remarkable performance in selective hydrogenation of 1,3-butadiene. J. Am. Chem. Soc. *137*, 10484–10487.

38. Moller, K., Koningsberger, D.C., and Bein, T. (1989). Stabilization of metal ensembles at room temperature: palladium clusters in zeolites. J. Phys. Chem. *93*, 6116–6120.

39. Xu, L., Zhang, Z., and Sachtler, W.M.H. (1992). Effect of zeolite protons on Pd particle size and H_2 chemisorption. J. Chem. Soc. Faraday Trans. *88*, 2291–2295.

40. Yan, J., Fan, Z., Sun, W., Ning, G., Wei, T., Zhang, Q., Zhang, R., Zhi, L., and Wei, F. (2012). Advanced asymmetric supercapacitors based on $Ni(OH)_2$/graphene and porous graphene electrodes with high energy density. Adv. Funct. Mater. *22*, 2632–2641.

41. Tedsree, K., Li, T., Jones, S., Chan, C.W.A., Yu, K.M.K., Bagot, P.A.J., Marquis, E.A., Smith, G.D.W., and Tsang, S.C.E. (2011). Hydrogen production from formic acid decomposition at room temperature using a Ag-Pd core-shell nanocatalyst. Nat. Nanotech. *6*, 302–307.

42. Jiang, K., Xu, K., Zou, S., and Cai, W.-B. (2014). B-doped Pd catalyst: boosting room-temperature hydrogen production from formic acid-formate solutions. J. Am. Chem. Soc. *136*, 4861–4864.

43. Song, F.-Z., Zhu, Q.-L., Tsumori, N., and Xu, Q. (2015). Diamine-alkalized reduced graphene oxide: immobilization of sub-2 nm palladium nanoparticles and optimization of catalytic activity for dehydrogenation of formic acid. ACS Catal. *5*, 5141–5144.

44. Zhang, S., Metin, Ö., Su, D., and Sun, S. (2013). Monodisperse AgPd alloy nanoparticles and their superior catalysis for the dehydrogenation of formic acid. Angew. Chem. Int. Ed. *52*, 3681–3684.

45. Bi, Q.-Y., Du, X.-L., Liu, Y.-M., Cao, Y., He, H.-Y., and Fan, K.-N. (2012). Efficient subnanometric gold-catalyzed hydrogen generation via formic acid decomposition under ambient conditions. J. Am. Chem. Soc. *134*, 8926–8933.

46. Tsuchiya, H., and Kobayashi, O. (2004). Mass production cost of PEM fuel cell by learning curve. Int. J. Hydrogen Energy *29*, 985–990.

47. Zhou, X., Huang, Y., Xing, W., Liu, C., Liao, J., and Lu, T. (2008). High-quality hydrogen from the catalyzed decomposition of formic acid by Pd-Au/C and Pd-Ag/C. Chem. Commun. 3540–3542.

48. Shi, X.R., and Sholl, D.S. (2012). Nucleation of Rh_n($n = 1-5$) clusters on γ-Al_2O_3 surfaces: a density functional theory study. J. Phys. Chem. C *116*, 10623–10631.

49. Li, J., Croiset, E., and Sandoval, L.R. (2013). Effect of metal–support interface during CH_4 and H_2 dissociation on Ni/γ-Al_2O_3: a density functional theory study. J. Phys. Chem. C *117*, 16907–16920.

50. Zhang, S.T., Li, C.M., Yan, H., Wei, M., Evans, D.G., and Duan, X. (2014). Density functional theory study on the metal–support interaction between Ru cluster and anatase TiO_2(101) surface. J. Phys. Chem. C *118*, 3514–3522.

51. Kacprzak, K.A., Czekaj, I., and Mantzaras, J. (2012). DFT studies of oxidation routes for Pd9 clusters supported on γ-alumina. Phys. Chem. Chem. Phys. *14*, 10243–10247.

52. Luo, Q., Feng, G., Beller, M., and Jiao, H.J. (2012). Formic acid dehydrogenation on Ni(111) and comparison with Pd(111) and Pt(111). J. Phys. Chem. C *116*, 4149–4156.

53. Wang, Y., Qi, Y., Zhang, D., and Liu, C. (2014). New insight into the decomposition mechanism of formic acid on Pd(111): competing formation of CO_2 and CO. J. Phys. Chem. C *118*, 2067–2076.

54. Cho, J., Lee, S., Han, J., Yoon, S.P., Nam, S.W., Choi, S.H., Lee, K.Y., and Ham, H.C. (2014). Importance of ligand effect in selective hydrogen formation via formic acid decomposition on the bimetallic Pd/Ag catalyst from first-principles. J. Phys. Chem. C *118*, 22553–22560.

55. Yu, H., Wei, X., Li, J., Gu, S., Zhang, S., Wang, L., Ma, J., Li, L., Gao, Q., Si, R., et al. (2015). The XAFS beamline of SSRF. Nucl. Sci. Tech. *26*, 050102.

56. Kresse, G., and Furthmülle, J. (1996). Efficient iterative schemes for *ab initio* total-energy calculations using a plane-wave basis set. Phys. Rev. B *54*, 11169–11186.

57. Blochl, P.E. (1994). Projector augmented-wave method. Phys. Rev. B *50*, 17953–17979.

58. Kresse, G., and Joubert, D. (1999). From ultrasoft pseudopotentials to the projector augmented-wave method. Phys. Rev. B *59*, 1758–1775.

59. Perdew, J.P., Burke, K., and Ernzerhof, M. (1996). Generalized gradient approximation made simple. Phys. Rev. Lett. *77*, 3865–3868.